

Strongly three-dimensional electronic structure and Fermi Surfaces of $\text{SrFe}_2(\text{As}_{0.65}\text{P}_{0.35})_2$: Comparison with $\text{BaFe}_2(\text{As}_{1-x}\text{P}_x)_2$

H. Suzuki¹, T. Kobayashi², S. Miyasaka^{2,6}, T. Yoshida^{1,6}, K. Okazaki¹, L. C. C. Ambolode II¹, S. Ideta¹, M. Yi³, M. Hashimoto⁴, D. H. Lu⁴, Z.-X. Shen⁴, K. Ono⁵, H. Kumigashira⁵, S. Tajima^{2,6} and A. Fujimori^{1,6}

¹*Department of Physics, University of Tokyo, Bunkyo-ku, Tokyo 113-0033, Japan*

²*Department of Physics, Osaka University, Toyonaka, Osaka 560-8531, Japan*

³*Stanford Institute of Materials and Energy Sciences, Stanford University, Stanford, CA 94305, USA*

⁴*Stanford Synchrotron Radiation Lightsource, SLAC National Accelerator Laboratory, Menlo Park, CA 94305, USA*

⁵*KEK, Photon Factory, Tsukuba, Ibaraki 305-0801, Japan and*

⁶*JST, Transformative Research-Project on Iron Pnictides (TRIP), Chiyoda, Tokyo 102-0075, Japan*

(Dated: April 5, 2018)

The isovalent-substituted iron-pnictide superconductor $\text{SrFe}_2(\text{As}_{1-x}\text{P}_x)_2$ ($x=0.35$) has a slightly higher optimum critical temperature than the similar system $\text{BaFe}_2(\text{As}_{1-x}\text{P}_x)_2$, and its parent compound SrFe_2As_2 has a much higher Néel temperature than BaFe_2As_2 . We have studied the band structure and the Fermi surfaces of optimally-doped $\text{SrFe}_2(\text{As}_{1-x}\text{P}_x)_2$ by angle-resolved photoemission spectroscopy (ARPES). Three holelike Fermi surfaces (FSs) around (0,0) and two electronlike FSs around (π,π) have been observed as in the case of $\text{BaFe}_2(\text{As}_{1-x}\text{P}_x)_2$. Measurements with different photon energies have revealed that the outermost hole FS is more strongly warped along the k_z direction than the corresponding one in $\text{BaFe}_2(\text{As}_{1-x}\text{P}_x)_2$, and that the innermost one is an ellipsoidal pocket. The electron FSs are almost cylindrical unlike corrugated ones in $\text{BaFe}_2(\text{As}_{1-x}\text{P}_x)_2$. Comparison of the ARPES data with first-principles band-structure calculation revealed that the quasiparticle mass renormalization factors are different not only between bands of different orbital character but also between the hole and electron FSs of the same orbital character. By examining nesting conditions between the hole and electron FSs, we conclude that magnetic interactions between FeAs layers rather than FS nesting play an important role in stabilizing the antiferromagnetic order. The insensitivity of superconductivity to the FS nesting can be explained if only the d_{xy} and/or $d_{xz/yz}$ orbitals are active in inducing superconductivity or if FS nesting is not important for superconductivity.

PACS numbers: 74.25.Jb, 71.18.+y, 74.70.Xa, 71.38.Cn

I. INTRODUCTION

Since the discovery of high temperature superconductivity in iron pnictides, the mechanism of Cooper pairing and the symmetry of the order parameter have been intensely debated. Among them the $\text{BaFe}_2(\text{As}_{1-x}\text{P}_x)_2$ (Ba122P) system¹ has attracted particular attention since the presence of line nodes in the superconducting (SC) order parameter was suggested experimentally²⁻⁴. In the framework of the spin-fluctuation (SF)-mediated superconductivity mechanism, the intra-orbital nesting between hole and electron Fermi surfaces (FSs) brings about a sign-changing s^\pm -wave SC state^{5,6}. A suggested location is horizontal line nodes on the hole FS around the Z point^{7,8}. On the other hand, in the framework of the orbital-fluctuation-mediated superconductivity mechanism, inter-orbital nesting between hole and electron FSs enhances antiferro-orbital fluctuation and a s^{++} -wave SC state without sign change will be realized⁹⁻¹¹. If both spin and orbital fluctuations are important, more complicated line nodes such as loop nodes have been predicted¹². A loop-like node in the electron FS is also suggested based on a Raman scattering experiment¹³ and from the viewpoint of the hybridization between two electron pockets¹⁴. In order to identify the pairing mechanism, systematic studies of the FS shapes and their orbital character are necessary. For this

purpose, $\text{SrFe}_2(\text{As}_{1-x}\text{P}_x)_2$ (Sr122P), which is closely related to Ba122P, is an interesting system to study how the changes in the crystal structure affect the electronic, magnetic, and superconducting properties.

The phase diagrams of Ba122P and Sr122P are compared with each other in Fig. 1 (a)^{15,16}. The Néel temperature (T_N) of the parent compound SrFe_2As_2 is 197 K, which is as much as 50 K higher than that of BaFe_2As_2 , and T_N is higher in Sr122P than in Ba122P in the doping range $x < 0.3$, where antiferromagnetic (AFM) order is present. In the same way as Ba122P, superconductivity in Sr122P appears as the AFM order is suppressed by P substitution¹⁷. The superconducting transition temperature (T_c) of Sr122P reaches up to 30 K (as grown) or 33 K (annealed) at $x = 0.35$ ¹⁸, which are comparable to, or higher than, $T_c = 30$ K of $\text{BaFe}_2(\text{As}_{0.7}\text{P}_{0.3})_2$. Superconductivity appears in the range $0.25 < x < 0.5$ for Sr122P, which is narrower than $0.13 < x < 0.74$ for Ba122P.

The existence of line nodes is experimentally suggested in Sr122P as well. ³¹P-NMR and specific heat measurements show that Sr122P has a large residual DOS in as-grown samples below T_c ¹⁷. It was also found that annealing decreases the residual electronic specific heat coefficient at $T = 0$, γ_r , and changes the magnetic field (H) dependence of γ_r from sublinear $\gamma_r \propto H^{0.7}$ to H linear $\gamma_r \propto H$ ¹⁸. These changes can be considered as a transition from a dirty to clean superconductor with

reduced defect concentration.

The effect of replacing Ba atoms by smaller Sr atoms can be observed in the changes of the lattice parameters. Figures 1(b)-(d) show the doping dependence of the a - and c -axis parameters, and the pnictogen height h_{pn} , respectively^{1,15,18–20}. All of them monotonically decrease as the doping level x increases. Reflecting the smaller atomic radius of Sr atoms than Ba, the a -axis is slightly shorter and the c -axis is about 0.8 Å shorter in Sr122P. On the other hand, h_{pn} , which is considered to be correlated with T_c ²¹, is almost the same in both systems. These results indicate that the main structural difference between Sr122P and Ba122P is the spacing between FeAs layers or the As-As distance in the c -direction, which may lead to different coupling strengths between the FeAs layers along along the c -axis.

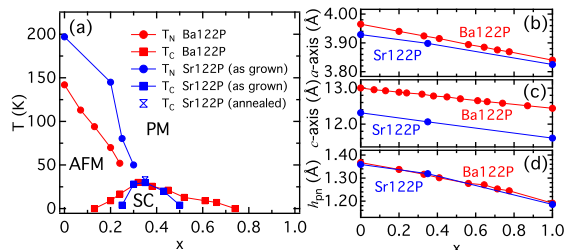


FIG. 1: (Color online) (a) Phase diagrams of $\text{BaFe}_2(\text{As}_{1-x}\text{P}_x)_2$ (Ba122P)¹⁵ and as-grown $\text{SrFe}_2(\text{As}_{1-x}\text{P}_x)_2$ (Sr122P)^{16,18}. AFM, PM, SC stand for the antiferromagnetic, paramagnetic, and superconducting phases, respectively. (b), (c) Comparison of the a - and c -axis lattice constants. (d) Comparison of the pnictogen height h_{pn} . Data are taken from Refs. 1,15,18–20.

In the present study, we have performed ARPES measurements of optimally-doped Sr122P ($T_c = 30$ K, $x = 0.35$, as grown) and compared the results with those of Ba122P²² in order to elucidate the dependence of the band structure and FS shapes on the lattice parameters. ARPES data are compared with local-density-approximation (LDA) band-structure calculations in order to estimate the quasiparticle mass renormalization factors. We shall also discuss the importance of inter/intra-orbital nesting conditions from the obtained FS shapes and their orbital character.

II. METHODS

Sr122P ($x=0.35$) single crystals were prepared by the self-flux method described in Ref. 18. $T_c = 30$ K was determined from the onset of Meissner diamagnetic signal with a transition width $\Delta T_c \simeq 5$ K. We have also measured annealed samples and observed the same band structures and FSs. Some bands were more clearly resolved in annealed samples²³. ARPES experiments were carried out at beamline 28A of Photon Factory (PF),

KEK, and beamline 5-4 of Stanford Synchrotron Radiation Lightsource (SSRL). In order to obtain fresh surfaces, all samples were cleaved *in situ* at pressure better than 1×10^{-10} Torr. Cleavage occurs along the ab planes. The samples were cleaved and kept at $T = 10$ K during the measurements. There was no sign of sample degradation during experiments of ~ 24 hours. The kinetic energy and the momentum of photoelectrons were measured using Scienta SES2002 and R4000 electron energy analyzers at PF and SSRL, respectively. In-plane (k_x, k_y) and out-of-plane momenta (k_z) are expressed in units of π/a and $2\pi/c$, where $a = 3.90$ Å and $c = 12.09$ Å are the in-plane and out-of-plane lattice constants. Here, the X, Y axes point from Fe towards the second nearest neighbor Fe atoms and the z axis is parallel to the c -axis. Calibration of the Fermi level (E_F) was achieved using spectra of gold which was in electrical contact with the samples. Incident photon energy from 24 eV to 88 eV were linearly polarized. The energy resolution was $\Delta E \sim 5$ meV.

In order to study the orbital character of the observed bands and the effect of replacing Ba by Sr in Ba122P, we have performed LDA band-structure calculations using Wien2k package²⁴. The x and y axes point from Fe towards the nearest neighbor Fe atoms. The calculations were done using the experimentally determined tetragonal lattice constants a, c and the pnictogen heights h_{pn} . The lattice parameters used in the calculations (in units of Å) are $a = 3.92$, $c = 12.76$, $h_{pn} = 1.29$ for Ba122P and $a = 3.90$, $c = 12.09$, $h_{pn} = 1.31$ for Sr122P. The calculations are done for the parent compounds Ba122 and Sr122 using the crystal structural parameters for $x = 0.35$ because the band structures were almost identical for BaFe_2As_2 and BaFe_2P_2 if the same crystal structures were used.

III. RESULTS AND DISCUSSION

In-plane Fermi surface mapping is shown in Figs. 2 (a) and (b). Sr122P has a space group symmetry of $I4/mmm$ and its first Brillouin zone is shown in the inset of (a). Changing the photoemission angle θ and ϕ with a fixed photon energy $h\nu$ corresponds to an approximately constant k_z plane in the momentum space. There are three hole-like bands crossing E_F around the Z point [Fig. 2 (c)], while two hole-like bands cross E_F around the Γ point [Fig. 2 (e)]. There are two electron-like bands crossing E_F around the X point [Fig. 2 (d)]. We shall discuss the orbital character of the FSs in the following paragraph. The difference of the intensities within the hole FSs around the Z point and the difference between the two identical electron pockets at (1,1) and (-1,1) are due to matrix-element effects arising from the geometrical setup of the experiment.

ARPES E - k intensity plots around high-symmetry cuts are shown in Figs. 2 (c)-(e). By taking the second derivatives of the ARPES intensity, we have deter-

mined the peak positions of the multiple bands near E_F (see Supplemental Material²³). These peaks are fitted to parabolic dispersions of the form $E(\mathbf{k}) = E(0) + \frac{\hbar^2 k^2}{2m^*}$ and the quasiparticle mass m^*/m_e is deduced. These values are shown in the inset of Figs. 2 (c)-(e). We shall discuss below the electron correlation strength by comparing the ARPES data with LDA band-structure calculation results.

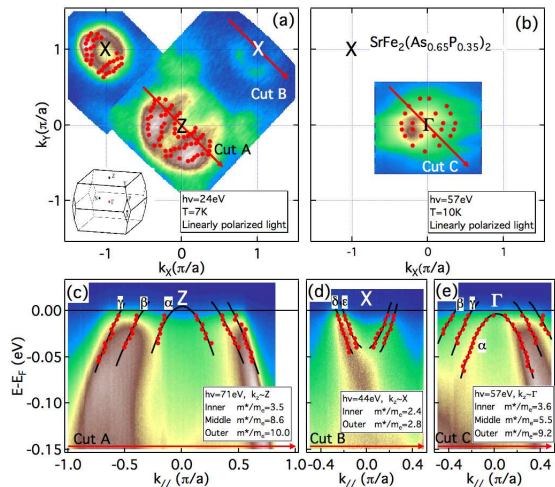


FIG. 2: (Color online) (a),(b) In-plane Fermi surface (FS) mapping for Sr122P ($x = 0.35$) taken at $h\nu = 24$ eV [(a)] and 57 eV [(b)]. Filled circles indicate the k_F positions. The first Brillouin zone of Sr122P is shown in the inset of panel (a). (c)-(e) ARPES intensity plot taken along the cuts shown in (a) and (b).

Figure 3 shows FS mapping along the k_z direction taken with 30-90 eV photons. The relationship between the excitation energy and the k_z position is given by the formula $k_z = \sqrt{\frac{2m}{\hbar^2}[(h\nu - \Phi) \cos^2 \theta + V_0]}$, where $h\nu$ is the photon energy, Φ is the work function, and V_0 is the inner potential²⁵. V_0 is set to 13.5 eV for Ba122P and 14 eV for Sr122P in order to best reproduce the periodicity of the hole FS along the k_z direction. The dotted curves in Fig. 3 represent the FS shapes determined by fitting k_F positions. We call the inner, middle, and outer hole FSs around the Z point as α , β , and γ FSs, and the inner and outer electron FSs as ϵ and δ FSs, respectively. (The α FS of Ba122P was not visible in Ref. 22.) In Sr122P, the γ FS, which has strong d_{z^2} character around the Z point, shrinks rapidly as it approaches the Γ point. At the same time, the innermost α band shrinks and splits into two pockets. This is in contrast to that of Ba122P, in which all the hole FSs are connected in the entire k_z region. The stronger three-dimensionality in Sr122P originates from enhanced interlayer hopping matrix elements due to the smaller c -axis lattice constant.

The carrier number per Fe atom calculated from the FS volumes of Sr122P are $n_\alpha = 0.041$, $n_\beta = 0.64$, $n_\gamma = 0.81$ (hole FSs), $n_\delta = 0.39$ and $n_\epsilon = 0.18$ (electron FSs), re-

spectively. Although Sr122P is an isovalently substituted material, the total hole number $n_h = 1.49$ estimated from ARPES is larger than the total electron number $n_e = 0.57$.

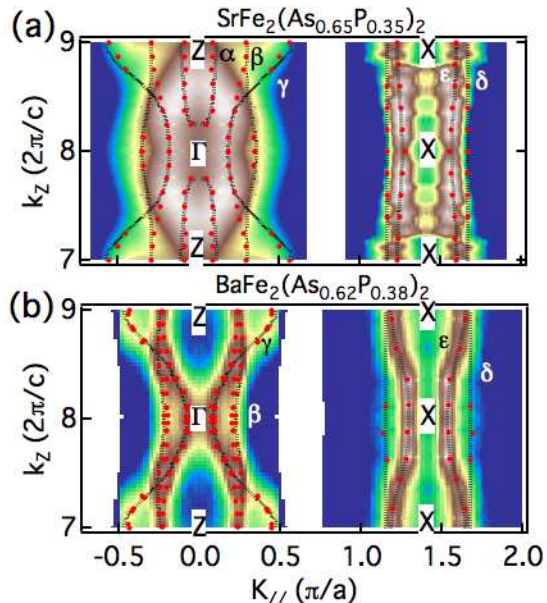


FIG. 3: (Color online) Fermi surface mapping taken in the k_z - k_{\parallel} plane for Sr122P ($x = 0.35$) [(a)] and Ba122P ($x = 0.38$)²² [(b)]. In Sr122P, the γ FS is warped more strongly than that of Ba122P and the α FS forms a 3D ellipsoidal hole pocket. The electron FSs ϵ and δ are less warped and nearly cylindrical-like.

Figure 4 shows the LDA band structures and FSs of Sr122P and Ba122P ($x = 0.35$). Around the Γ point, the calculation predicts that two $d_{xz/yz}$ and one d_{xy} hole bands cross E_F in both systems. However, in the ARPES data of Sr122P [Fig. 2 (e)], the innermost band of d_{xy} sinks slightly below E_F . The lowering of the α band by electron correlation probably causes this discrepancy. Around the Z point, three hole bands with d_{xy} (inner), $d_{xz/yz}$ (middle), and d_{z^2} (outer) orbital character, cross E_F , consistent with the ARPES data [Fig. 2 (c)]. The larger radius of the outer d_{z^2} hole FS in Sr122P than that in Ba122P is also reproduced by the experiment. Around the X point, the orbital characters of the two electron FSs (d_{xy} , $d_{xz/yz}$) along the Γ -X line are interchanged between the two systems.

Comparison between the ARPES data and the LDA band-structure calculation enables us to evaluate the quasiparticle mass renormalization factor. Table I summarizes the orbital character, m^*/m_e , m_b/m_e , and m^*/m_b of the bands near E_F , where m^* is the effective mass, m_b is the band mass, and m_e is the free-electron mass. The masses listed here are the values estimated along the Γ -X line for the FSs around the Γ and X points, and along the Z-X line for the FSs around the Z point by fitting the ARPES and LDA band to

parabolic dispersions as shown in Fig. 2. The m^*/m_b values for Ba122P ($x = 0.38$) are also shown as reference when direct comparison is possible²⁶. The m^*/m_e values vary from 1.6 to 8.0 for Sr122P, and are larger than those of Ba122P, 1.2-5.5. The larger values of Sr122P may indicate stronger quantum critical fluctuations than in Ba122P²⁷. A dynamical-mean-field-theory (DMFT) study²⁸ predicts a positive correlation between the magnitude of the ordered magnetic moments and the mass renormalization of quasiparticles. The stronger renormalization in Sr122P with the higher T_N is consistent with this trend.

Regarding the orbital dependence of mass enhancement, the DMFT calculation²⁸ predicts that the enhancement is stronger for the t_{2g} orbitals, d_{xy} , d_{yz} , and d_{zx} , than for the e_g orbitals, d_{z^2} and $d_{x^2-y^2}$, and is the strongest for d_{xy} . The strongest mass enhancement among the iron pnictides and chalcogenides, $m^*/m_b \sim 7$, takes place in the d_{xy} orbital in FeTe, while the mass enhancement for $d_{xz/yz}$ in FeTe is ~ 5 . The orbital dependence of mass enhancement in Sr122P obtained here seems to follow this general trend, whereas the magnitudes are larger than the DMFT prediction in the $d_{xz/yz}$ orbital on the β FS around the Γ point, and in the d_{xy} orbital on the ϵ FS around the X point. This difference indicates that each FS has different mass enhancement factors even for the same orbital character. Considering that the mass renormalization is expected to be enhanced by the scattering of quasiparticles between electron and hole FSs, the strong mass enhancement of the hole and electron FSs with different orbital character may imply the importance of inter-orbital scattering process.

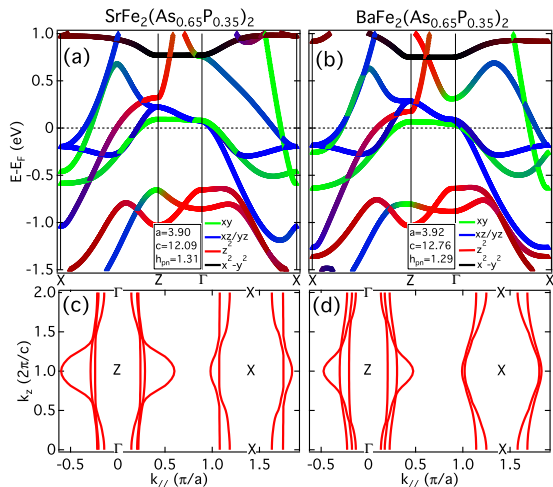


FIG. 4: (Color online) (a),(b) LDA band structures and their orbital character for Sr122P [(a)] and Ba122P [(b)] ($x=0.35$). The lattice parameters are shown in the inset. (c),(d) Calculated FSs of Sr122P [(c)] and Ba122P [(d)].

The FS shapes and their orbital character of Sr122P are summarized in Fig. 5. FSs of the same orbital character are connected by the antiferromagnetic ordering

TABLE I: Mass renormalization factors for the FSs of SrFe₂(As_{0.65}P_{0.35})₂. m^* is the effective mass, m_b is the bare band mass, and m_e is the free-electron mass. The values of m^*/m_e and m_b/m_e have been estimated by fitting the bands obtained from the ARPES (Fig. 2) and the LDA calculations to parabolic dispersions in the range $|E(\mathbf{k})| < 0.05$ eV. m^*/m_b values for Ba122P ($x = 0.38$) are also shown in parentheses when corresponding bands exist²⁶. Mass values for the anisotropic δ and ϵ FSs are calculated along the Γ -X line.

k_z FS	Orbital	m^*/m_e	m_b/m_e	m^*/m_b
Γ	β $d_{xz/yz}$	9.2 (3.8)	1.6 (1.4)	5.8 (2.7)
	γ $d_{xz/yz}$	5.5 (2.6)	0.88 (0.72)	6.3 (3.6)
Z	α d_{xy}	3.5	1.8	1.9
	β $d_{xz/yz}$	8.6 (2.5)	1.2 (1.2)	7.2 (2.0)
	γ d_{z^2}	10.0 (3.9)	2.7 (3.2)	3.7 (1.2)
X	ϵ d_{xy}	2.4 (1.9)	0.30 (0.35)	8.0 (5.5)
	δ $d_{xz/yz}$	2.8 (1.0)	1.8 (0.56)	1.6 (1.8)

vector $\mathbf{Q} = (\pi/a, \pi/a, 2\pi/c)^{6,21,29}$. Also, inter-orbital nesting between the $d_{xz/yz}$ and d_{xy} orbitals, which enhances the antiferro-orbital fluctuation and brings about the large enhancement of the susceptibility in the charge channel^{10,11,30}, is shown by wavy lines. On the $k_z \sim 0$ plane, both hole FSs are of $d_{xz/yz}$ character and the α FS of d_{xy} character is absent. On the $k_z \sim 2\pi/c$ plane [Fig. 5 (b)], the inner FS of d_{xy} character is smaller than that in Ba122P ($x = 0.30$)³¹ and the outer FS of d_{z^2} character is larger due to the enhanced three-dimensionality. This modification in the FS radii deteriorate the intra-orbital nesting properties within the d_{xy} orbital as compared with those in Ba122P. Besides, the effects of inter-orbital scattering seems to be also weaker in Sr122P, since the inter-orbital nesting properties between the enlarged d_{z^2} FS and other FSs, and between the small ellipsoidal d_{xy} FS and other FSs are worse.

From this comparison we gain several insights into the origin of the AFM order and the superconductivity in the P-doped 122 systems. As for the AFM order, if the AFM order is described by the nesting-driven spin density wave, T_N should be lower in Sr122P; however, T_N is always higher in Sr122P as shown in Fig. 1 (a). We, therefore, suggest the importance of magnetic interaction between FeAs layers to explain the high T_N of Sr122P with the shorter c -axis length. A mechanism of inter-layer hybridization due to Fe-As-As-Fe hopping has indeed been suggested by Khodas *et al.*¹⁴. As for the superconductivity, although both inter- and intra-orbital nesting condition for the γ hole FS is significantly worse in Sr122P than in Ba122P, $T_c = 33$ K for annealed Sr122P samples is slightly higher than Ba122P; this can be explained if the d_{xy} and/or $d_{xz/yz}$ are active while the d_{z^2} orbital is not inducing superconductivity or if FS nesting is not important for superconductivity.

Finally, we comment on the suppression rates of T_N and T_c by P substitution³². In the underdoped region ($x < 0.3$), T_N is more rapidly suppressed in Sr122P

($-dT_N/dx \sim 480\text{K}/x$) than in Ba122P ($\sim 360\text{K}/x$). Also, in the overdoped region ($x > 0.3$), T_c is more rapidly suppressed in Sr122P ($-dT_c/dx \sim 94\text{K}/x$) than in Ba122P ($\sim 75\text{K}/x$). These results indicate that the random potential induced by P substitution is stronger in Sr122P than in Ba122P. This is probably because substituted P atoms in the more closely spaced FeAs layers [see Fig. 1 (c)] disturb the potential in the FeAs layers more strongly. In spite of the stronger impurity potential, T_c is higher in Sr122P; this may be because the FS shapes with poorer nesting are more favorable to superconductivity, but further studies are necessary to clarify this issue.

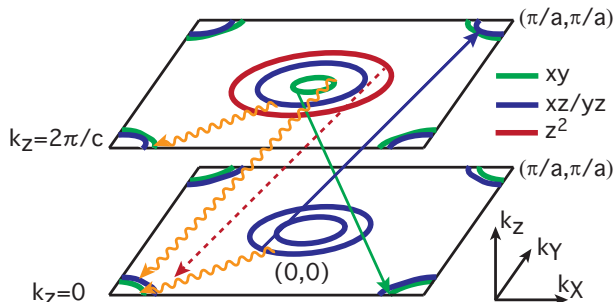


FIG. 5: (Color online) Schematic presentation of the FS shapes and the orbital character on the $k_z \sim 0$ plane and the $k_z \sim 2\pi/c$ plane for Sr122P ($x = 0.35$). The orbital character is determined by comparing the ARPES data and the LDA calculation. Antiferromagnetic fluctuations with wave vector $(\pi/a, \pi/a, 2\pi/c)$ shown by solid arrows scatter quasi-particles between the electron and hole FSs of the same orbital character^{6,21,29}. Since the d_{z^2} band does not cross E_F around the zone corner, it does not contribute to the pairing through the spin-fluctuation channel (dotted arrow). Wavy lines indicate nesting between FSs of different orbital character ($d_{xz/yz}$ and d_{xy}), which gives rise to orbital fluctuations and a finite SC gap on the d_{z^2} FS^{10,11,30,31}.

IV. CONCLUSION

We have performed ARPES measurements on the isovalent-substituted iron pnictide superconductor

Sr122P and compared the results with those of Ba122P. The outer hole FS of d_{z^2} character is strongly warped along the k_z direction than that of Ba122P. The dramatic change of the FS shapes induced by the replacement of Ba by Sr highlights the sensitiveness of the electronic structure on the c -axis parameter. Comparison of ARPES data with LDA band-structure calculations has revealed that quasiparticle mass is strongly renormalized and that the renormalization factors on the electron and hole FSs are different even within the same orbital. This may indicate that quasi-particles are scattered between electron and hole FSs of different orbital character. We have also examined nesting conditions between the hole FSs at the zone center and the electron FSs at the zone corner. The high T_N of Sr122P in spite of the weaker intra/inter-orbital nesting indicates that the interlayer magnetic interactions play a more important role than FS nesting in stabilizing the AFM order. Also, despite the significantly worse nesting of the d_{z^2} FS in Sr122P, $T_c = 33$ K is slightly higher than that of Ba122P. This can be explained if only d_{xy} and/or $d_{xz/yz}$ orbitals participate in superconductivity or if FS nesting is not important for superconductivity. These results impose restriction on microscopic theories and requires them to naturally reproduce the high T_c of Ba/Sr122P and iron pnictides in general.

We are grateful to M. Nakajima and H. Eisaki for enlightening discussions and for providing phase diagram data of Ba122P. The Stanford Synchrotron Radiation Lightsource is operated by the Office of Basic Energy Science, US Department of Energy. Experiment at Photon Factory was approved by the Photon Factory Program Advisory Committee (Proposal No. 2009S2-005 and 2012G075). H.S. acknowledges financial support from Advanced Leading Graduate Course for Photon Science (ALPS).

¹ S. Kasahara, T. Shibauchi, K. Hashimoto, K. Ikada, S. Tonegawa, R. Okazaki, H. Shishido, H. Ikeda, H. Takeya, K. Hirata, T. Terashima, and Y. Matsuda, Phys. Rev. B, **81**, 184519 (2010).
² Y. Nakai, T. Iye, S. Kitagawa, K. Ishida, S. Kasahara, T. Shibauchi, Y. Matsuda, and T. Terashima, Phys. Rev. B, **81**, 020503 (2010).
³ K. Hashimoto, M. Yamashita, S. Kasahara, Y. Senshu, N. Nakata, S. Tonegawa, K. Ikada, A. Serafin, A. Carrington, T. Terashima, H. Ikeda, T. Shibauchi, and Y. Matsuda, Phys. Rev. B, **81**, 220501 (2010).

⁴ M. Yamashita, Y. Senshu, T. Shibauchi, S. Kasahara, K. Hashimoto, D. Watanabe, H. Ikeda, T. Terashima, I. Vekhter, A. B. Vorontsov, and Y. Matsuda, Phys. Rev. B, **84**, 060507 (2011).
⁵ K. Kuroki, S. Onari, R. Arita, H. Usui, Y. Tanaka, H. Kontani, and H. Aoki, Phys. Rev. Lett., **101**, 087004 (2008).
⁶ A. Chubukov, Annu. Rev. Cond. Mat., **3**, 57 (2012).
⁷ K. Suzuki, H. Usui, and K. Kuroki, J. Phys. Soc. Jpn., **80**, 013710 (2011).
⁸ S. Graser, A. F. Kemper, T. A. Maier, H.-P. Cheng, P. J. Hirschfeld, and D. J. Scalapino, Phys. Rev. B, **81**, 214503

- (2010).
- ⁹ H. Kontani and S. Onari, Phys. Rev. Lett., **104**, 157001 (2010).
 - ¹⁰ S. Onari and H. Kontani, Phys. Rev. Lett., **109**, 137001 (2012).
 - ¹¹ T. Saito, S. Onari, and H. Kontani, Phys. Rev. B, **82**, 144510 (2010).
 - ¹² T. Saito, S. Onari, and H. Kontani, Phys. Rev. B, **88**, 045115 (2013).
 - ¹³ I. I. Mazin, T. P. Devereaux, J. G. Analytis, J.-H. Chu, I. R. Fisher, B. Muschler, and R. Hackl, Phys. Rev. B, **82**, 180502 (2010).
 - ¹⁴ M. Khodas and A. V. Chubukov, Phys. Rev. B, **86**, 144519 (2012).
 - ¹⁵ M. Nakajima, S. Uchida, K. Kihou, C.-H. Lee, A. Iyo, and H. Eisaki, J. Phys. Soc. Jpn., **81**, 104710 (2012).
 - ¹⁶ T. Kobayashi, S. Miyasaka, and S. Tajima, J. Phys. Soc. Jpn., **81SB**, SB045 (2012).
 - ¹⁷ T. Dulguun, H. Mukuda, T. Kobayashi, F. Engetsu, H. Kinouchi, M. Yashima, Y. Kitaoka, S. Miyasaka, and S. Tajima, Phys. Rev. B, **85**, 144515 (2012).
 - ¹⁸ T. Kobayashi, S. Miyasaka, S. Tajima, T. Nakano, Y. Nozue, N. Chikumoto, H. Nakao, R. Kumai, and Y. Murakami, Phys. Rev. B, **87**, 174520 (2013).
 - ¹⁹ S. R. Saha, K. Kirshenbaum, N. P. Butch, J. Paglione, and P. Y. Zavalij, Journal of Physics: Conference Series, **273**, 012104 (2011).
 - ²⁰ J. G. Analytis, C. M. J. Andrew, A. I. Coldea, A. McCollam, J.-H. Chu, R. D. McDonald, I. R. Fisher, and A. Carrington, Phys. Rev. Lett., **103**, 076401 (2009).
 - ²¹ K. Kuroki, H. Usui, S. Onari, R. Arita, and H. Aoki, Phys. Rev. B, **79**, 224511 (2009).
 - ²² T. Yoshida, I. Nishi, S. Ideta, A. Fujimori, M. Kubota, K. Ono, S. Kasahara, T. Shibauchi, T. Terashima, Y. Matsuda, H. Ikeda, and R. Arita, Phys. Rev. Lett., **106**, 117001 (2011).
 - ²³ See Supplemental Material at @ for details of ARPES spectra.
 - ²⁴ P. Blaha, K. Schwarz, G. K. H. Madsen, D. Kvasnicka, and J. Luitz, *WIEN2K, An Augmented Plane Wave + Local Orbitals Program for Calculating Crystal Properties* (Technische Universität Wien, Wien, Austria, 2001).
 - ²⁵ S. Hüfner, *Photoelectron Spectroscopy: Principles and Applications* (Springer, Berlin, 2003).
 - ²⁶ The m^*/m_e values are taken from Ref. 22. The m_b/m_e values are calculated from Fig. 2 (b).
 - ²⁷ K. Hashimoto, K. Cho, T. Shibauchi, S. Kasahara, Y. Mizukami, R. Katsumata, Y. Tsuruhara, T. Terashima, H. Ikeda, M. A. Tanatar, H. Kitano, N. Salovich, R. W. Giannetta, P. Walmsley, A. Carrington, R. Prozorov, and Y. Matsuda, Science, **336**, 1554 (2012).
 - ²⁸ Z. P. Yin, K. Haule, and G. Kotliar, Nat. Mater., **10**, 932 (2011).
 - ²⁹ A. F. Kemper, T. A. Maier, S. Graser, H.-P. Cheng, P. J. Hirschfeld, and D. J. Scalapino, New J. Phys., **12**, 073030 (2010).
 - ³⁰ H. Kontani, T. Saito, and S. Onari, Phys. Rev. B, **84**, 024528 (2011).
 - ³¹ T. Shimojima, F. Sakaguchi, K. Ishizaka, Y. Ishida, T. Kiss, M. Okawa, T. Togashi, C.-T. Chen, S. Watanabe, M. Arita, K. Shimada, H. Namatame, M. Taniguchi, K. Ohgushi, S. Kasahara, T. Terashima, T. Shibauchi, Y. Matsuda, A. Chainani, and S. Shin, Science, **332**, 564 (2011).
 - ³² S. Ishida, M. Nakajima, T. Liang, K. Kihou, C.-H. Lee, A. Iyo, H. Eisaki, T. Kakeshita, Y. Tomioka, T. Ito, and S. Uchida, J. Am. Chem. Soc., **135**, 3158 (2013).